Journal of Power Sources 414 (2019) 24–30

Contents lists available at ScienceDirect

Journal of Power Sources

journal homepage: www.elsevier.com/locate/jpowsour

Performance and stability of $SrCo_{0.9}Nb_{0.1}O_{3-\delta}$-$(La_{0.60}Sr_{0.40})_{0.95}(Co_{0.20}Fe_{0.80})O_{3-\delta}$ bilayer cathode for intermediate-temperature solid oxide fuel cells

Jie Wang[a,c], Tianrang Yang[b], Yeting Wen[b], Yang Zhang[a], Chunwen Sun[c], Kevin Huang[b,*]

[a] School of Materials Science and Engineering, University of Science and Technology Beijing, Beijing, 100083, China
[b] Department of Mechanical Engineering, University of South Carolina, Columbia, SC, 29201, USA
[c] Beijing Institute of Nanoenergy and Nanosystems, Chinese Academy of Sciences, Beijing, 100083, China

HIGHLIGHTS

- Demonstrated a stable and active bilayer cathode structure.
- Observed formation of $SrCO_3$ on the surface of top layer.
- Optimized the mass loading of the top layer.

ARTICLE INFO

Keywords:
Solid oxide fuel cells
Cathode
Polarization
Infiltration
Stability

ABSTRACT

Developing low-polarization and stable cathodes is key to the success of intermediate-temperature solid oxide fuel cells (IT-SOFCs). Here we report a study on the electrochemical performance and stability of a commercial $(La_{0.60}Sr_{0.40})_{0.95}(Co_{0.20}Fe_{0.80})O_{3-\delta}$ (LSCF) cathode overcoated by a $SrCo_{0.9}Nb_{0.1}O_{3-\delta}$ (SCN10) nanoscaled layer. At the optimal 20 wt% loading, the SCN10-LSCF bilayer cathode exhibits an 89.4% reduction in polarization resistance over the pristine LSCF at 650 °C. Over a 6,000-h testing at 650 °C, the SCN10-LSCF bilayer cathode also shows a similar stability to but much lower resistance than the pristine LSCF. A combined microscopic and spectroscopic post-test analysis unveils that SCN10-overcoat remains nanosized, well crystallized and uniformly distributed. An elongated, sporadically distributed phase was found and identified as $SrCO_3$ in the SCN10 layer, which may contribute to the degradation of SCN10-LSCF cathode.

1. Introduction

Solid oxide fuel cells (SOFCs) as a promising next-generation power generator have attracted century-long interest due to their high energy-efficiency, environmental benignity and excellent fuel flexibility [1–3]. Two remaining challenges to be addressed for a full commercialization of the SOFC technology are high product cost and poor reliability. A well-perceived strategy to address these two challenges is to lower SOFC's operating temperature from the current 700–800 °C to 600–650 °C. However, the realization of reduced-temperature SOFCs calls for the development of new low-polarization cathodes with high and sustainable oxygen reduction reaction (ORR) activity.

The state-of-the-art cathode currently adopted by the industry for 700–800 °C SOFCs is the mixed ionic and electronic conducting $La_xSr_{1-x}Co_{1-y}Fe_yO_{3-\delta}$ (LSCF) perovskites [4–7]. Introducing A-site deficiency in LSCF perovskite was also found to increase the ionic conductivity, electronic conductivity, as well as surface exchange of oxygen, due to the increased concentrations of oxygen vacancies and electronic holes [8–10]. Other mixed conducting perovskite or perovskite-related oxides such as $La_xSr_{1-x}CoO_{3-\delta}$ (LSCo) [11–13], $Ba_xSr_{1-x}Co_{1-y}Fe_yO_{3-\delta}$ (BSCF) [14], $SrCo_{1-x}B_xO_{3-\delta}$ (B=Nb, Ti, Ta, Mo, Sb, etc.) [15–21] and $LnBaCo_2O_{5+\delta}$ (Ln = Pr, Nd, Sm and Gd) [22–25] have a better ORR activity than LSCF, but cannot be directly employed as a bulk cathode due to their much higher thermal expansion coefficients (TECs). The only possible way to utilize these highly ORR-active perovskites for reduced-temperature SOFCs is to use them in the form of nanoparticles (NPs) anchored on a TEC-compatible skeleton, by which the high TEC of NPs would not negatively impact the mechanical integrity of the cell structure.

Therefore, a reasonable and practical approach to further enhancing the performance of industry-acceptable LSCF-based cathodes is to incorporate NPs of the highly ORR-active perovskite oxides into a porous LSCF structure. For SOFC developers, this approach is also deemed production friendly as it only adds a NP-incorporation step without

* Corresponding author.
E-mail address: huang46@cec.sc.edu (K. Huang).

https://doi.org/10.1016/j.jpowsour.2018.12.082
Received 23 October 2018; Received in revised form 17 December 2018; Accepted 28 December 2018
0378-7753/ © 2019 Elsevier B.V. All rights reserved.

significantly changing the current SOFC manufacturing process and adding too much cost.

In this study, we report on the performance of a commercial LSCF-based cathode covered by a nanoscaled $SrCo_{0.9}Nb_{0.1}O_{3-\delta}$ (SCN10) layer; the latter has been previously identified as a stable and active ORR catalyst at intermediate temperatures [15,16,26–29]. A long-term test up to 6000 h was particularly performed on such a SCN10-LSCF bilayer cathode, followed by an in-depth post-test analysis, to examine its suitability as a practical cathode for commercial SOFCs.

2. Experimental procedures

2.1. Preparation of LSCF symmetrical impedance cells

Symmetrical cells consisting of two identical porous LSCF thin film cathodes (LSCF-I: $(La_{0.60}Sr_{0.40})_{0.95}(Co_{0.20}Fe_{0.80})O_{3-\delta}$, Fuel Cell Materials) and a 300-μm thick, dense $Ge_{0.8}Gd_{0.2}O_{3-\delta}$ (GDC) electrolyte membrane were fabricated for impedance measurements. The dense GDC membrane was sintered at 1450 °C for 6 h in air; LSCF thin films were screen printed from a commercial ink (Fuel Cell Materials, LSCF-I) on both sides of GDC and calcined at 1100 °C for 2 h to remove the organic binder and achieve bonding to the electrolyte. The prepared cathode possesses a porous microstructure with an effective area of 1.27 cm^{-2} and thickness of ~25 μm.

2.2. Infiltrating SCN10 into the LSCF cathode

The SCN10 was incorporated into a pre-fabricated porous LSCF cathode scaffold through solution impregnation. All the reagents used to make the solution were in analytical grade. Briefly, stoichiometric amount of $Sr(NO_3)_2$, $Co(NO_3)_2{\cdot}6H_2O$ and $C_{10}H_5NbO_2{\cdot}xH_2O$ was dissolved in a distilled water, followed by adding citric acid 2 × the molar amount of total metal ions; a small amount of nitric acid was also added to reach a transparent solution. EDTA in equal molar amount of total metal ions was then added into the solution. The pH of the solution was adjusted to be around 8 by ammonia. The resultant solution was finally mixed with a dispersant Triton-X100. For each infiltration, approximately 10 μL solution was dropped onto each side of the porous LSCF cathode. A vacuum draw was then applied to promote a deeper penetration. Then, the sample was dried in an oven at 80 °C for 1 h, followed by a further calcination at 500 °C for 1 h. The infiltration process was then repeated until a desirable mass loading at 5, 10, 20 and 30 wt% was reached. Finally, the infiltrated cells were fired at 900 °C for 1 h to form the final perovskite phase of SCN10. Based on the electrode area, electrode thickness, mass of the cathode before/after impregnation and theoretical density of LSCF and SCN10, the electrode porosity can be estimated: 38%, 35%, 31%, 22% and 10% for the pristine LSCF, 5 wt% SCN10-LSCF, 10 wt% SCN10-LSCF, 20 wt% SCN10-LSCF and 30 wt% SCN10-LSCF, respectively.

To check phase purity of the infiltrated SCN10, we gradually dried out the solution at 80 °C to form a so-gel, which eventually ignited on the hot plate and resulted in a black powder. The black powder was then collected, crushed, and calcined in air at 900 °C for 1 h before X-ray diffraction was performed.

2.3. Materials characterization

Powder XRD patterns were collected over a 2θ range of 10–90 °C on an X-ray diffractometer (Rigaku) with Cu Kα radiation (λ = 1.5418 Å). The microstructures of the SCN10-LSCF cathodes were captured by a field emission scanning electron microscope (FESEM, Zeiss Ultraplus) and high-resolution transmission electron microscope (HR-TEM, JEM-2100F). The HAADF-STEM (Oxford X-max^{N}80T) equipped with EDS was also employed to obtain images and analyze chemical compositions.

2.4. Electrochemical analysis

Electrochemical impedance spectroscopy (EIS) was employed to evaluate the area-specific polarization resistance (R_P) of a symmetrical cell fabricated as a function of temperature in air; the instrument to perform EIS was a Solartron 1260 impedance analyzer coupled with 1287 electrochemical interface. The frequency was swept from 1 MHz to 0.01 Hz under a zero DC bias with an AC perturbation amplitude of 10 mV. The temperature dependence of R_P was studied from 650 to 800 °C with a 50 °C interval. In addition, long-term stability of R_P of both baseline and SCN-infiltrated cells was also evaluated at 650 °C for ~6,000 h. To minimize the variability, both cells were situated in the same furnace with a side-by-side configuration. Silver paste and mesh were used as the current collector for all the EIS measurements.

Anode-supported cells were used to evaluate the full cell performance of both pristine LSCF and 20 wt% SCN10-infiltrated sample. NiO (J.T. Baker), GDC10 ($Ce_{0.9}Gd_{0.1}O_{1.95}$, Fuelcell materials) and carbon black (Fisher Chemical) were ball milled for 3 h with ethanol in a weight ratio of 6:4:2; following by drying, pelletizing with 5 wt% PVB (Polyvinyl butyral, Sigma Aldrich) and firing at 800 °C for 2 h. The pellets were later used as anode substrates. Thin-film electrolyte were coated on the anode substrate with drop coating. 10 g GDC10 powder were ball milled in 28.5 g ethanol for 24 h with 0.4 g PVB as polymer binder, 0.3 g TEA (Trithanolamine, Alfa Aesar) as dispersant, 0.37 g PEG600 (polyethylene glycol-600, Alfa Aesar) and 0.37 g DBP (Dibutyl phthalate, Acros Organics) as plasticizer. 200 μL above slurry (corresponding with 40 μm-thickness) was added to the anode substrate drop by drop with a single-channel pipettor (100–1000 μL). It was then dried at room temperature for 2 h before sintering at 1500 °C for 6 h. The cathodes and current collectors were prepared following the same procedures with symmetrical cells. The cathode surface area was 0.35 cm^2. 3 vol% H_2O/97 vol% H_2 was supplied as fuel at a flow rate of 100 mL min^{-1} to the anode side; cathode was constantly exposed to static air. Current-voltage (IV) curves were measured from open circuit voltage (OCV) to 0.3 V at a sweep rate of 20 mV s^{-1}. The AC impedances were measured at OCV with a perpetuation voltage of 10 mV.

3. Results and discussion

3.1. Microstructure of the fabricated cells

The microstructures of the pristine LSCF and SCN10-LSCF cathodes were examined by FESEM, TEM and HRTEM, respectively. Fig. 1a (at lower magnifications) and 1f (at higher magnifications) show a porous well-connected pristine LSCF backbone network with a smooth surface. After infiltration, Fig. 1b–e (at lower magnifications) and Fig. 1g–j (at higher magnifications) depict a uniform and continuous coverage of SCN10 particles in size of 10–30 nm over the LSCF backbone. The higher the mass loading the more the coverage, as conceptually illustrated in Fig. 1k. An almost full coverage can be achieved at 20 wt% loading, even though some minor particle agglomerations are seen in the porous structure. More particle agglomeration and coarsening are observed at 30 wt% loading in Fig. 1e and j.

A TEM examination of 20 wt% SCN10-LSCF cathode is shown in Fig. 2a, further revealing that the SCN10 coverage layer is continuous and uniform with a thickness around 50 nm. The HRTEM images (insets of Fig. 2) show that both LSCF and SCN10 are well crystalized, consistent with the XRD results shown in Fig. 2d.

To further confirm the uniformity of SCN10-LSCF backbone surface, a high-angle annular dark-field scanning transmission electron microscopy (HAADF-STEM) as well as EDS elemental mapping were performed. Fig. 3 shows that the inner core exhibits a uniform distribution of La, Sr, Co, Fe, and O, corresponding to the LSCF phase. The absence of La and Fe elements and presence of Sr, Co, Nb and O elements on the outer layer confirm it as the SCN10 phase, further showing that SCN10 has been successfully incorporated onto outer surfaces of the LSCF

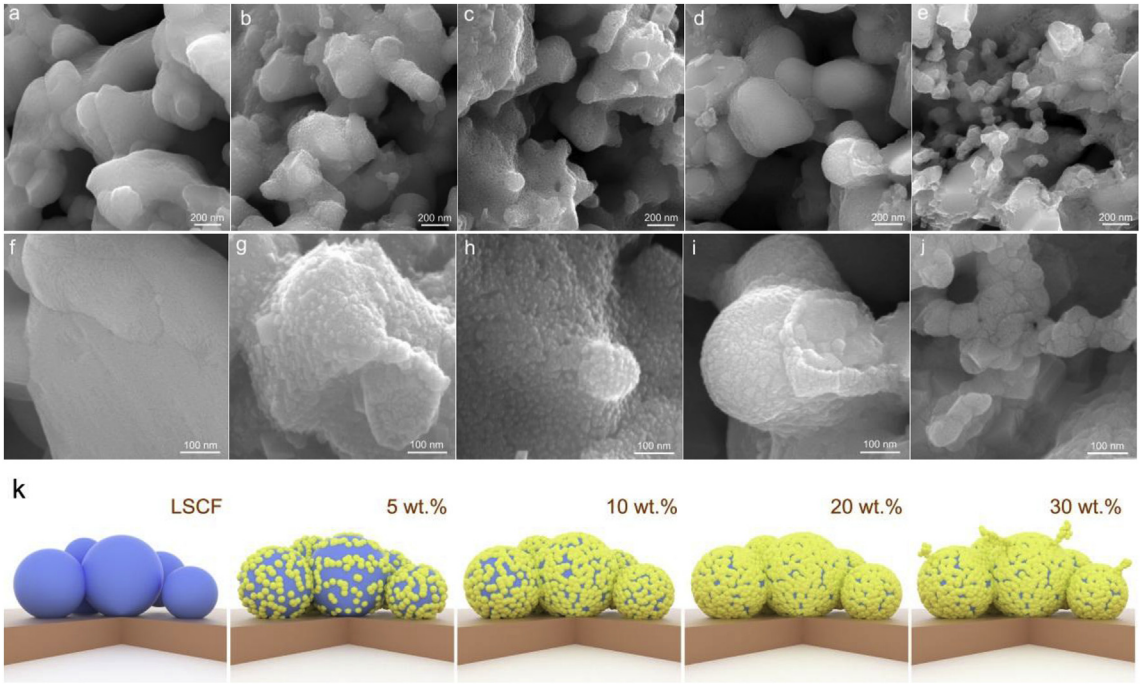


Fig. 1. SEM images showing the pristine porous LSCF backbone (a, f), and SCN10-NPs decorated LSCF cathodes at different mass loadings: (b, g) 5 wt%; (c, h) 10 wt %; (d, i) 20 wt%; (e, j) 30 wt%; (k) schematic illustration of the SCN10-LSCF porous cathode at different mass loadings.

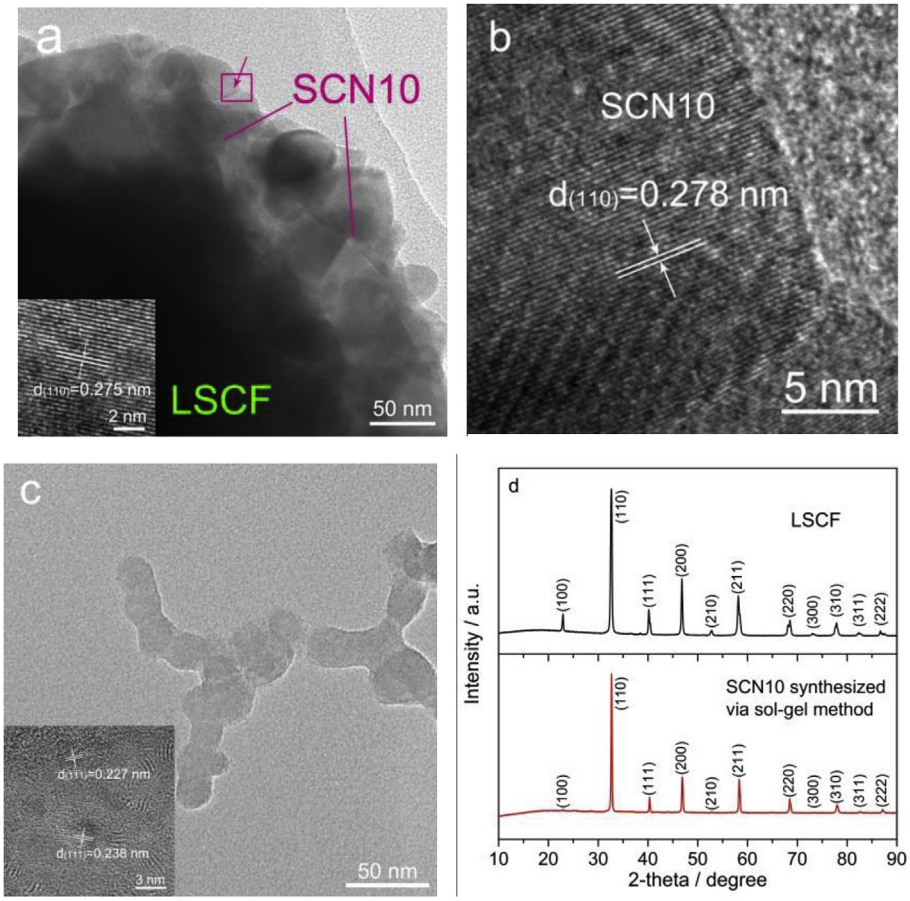


Fig. 2. TEM images showing (a) SCN10-LSCF cathode with 20 wt% mass loading; (b) HRTEM image of the selected region in Fig. 2a; (c) the aggregated individual SCN10-NPs in the SCN10-LSCF cathode. (d) XRD patterns of the LSCF from the commercial LSCF ink after 1100 °C calcination and SCN10 synthesized by sol-gel method. Insets in (a) and (c) are HRTEM images for the LSCF backbone and SCN10, respectively.

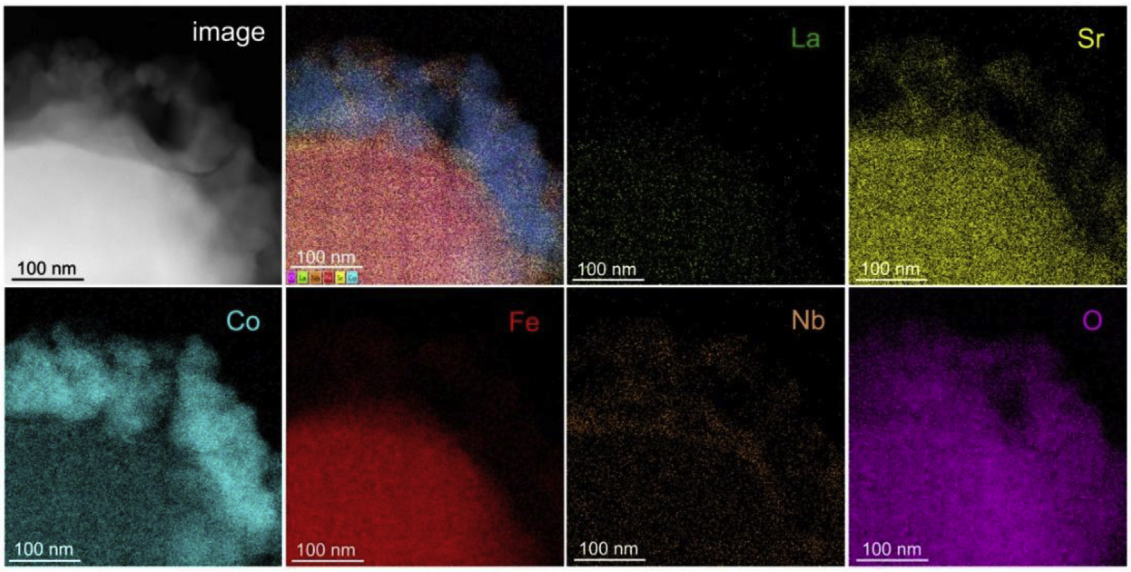


Fig. 3. The HAADF-STEM image and corresponding EDS elemental mapping of 20 wt% SCN10-LSCF cathode.

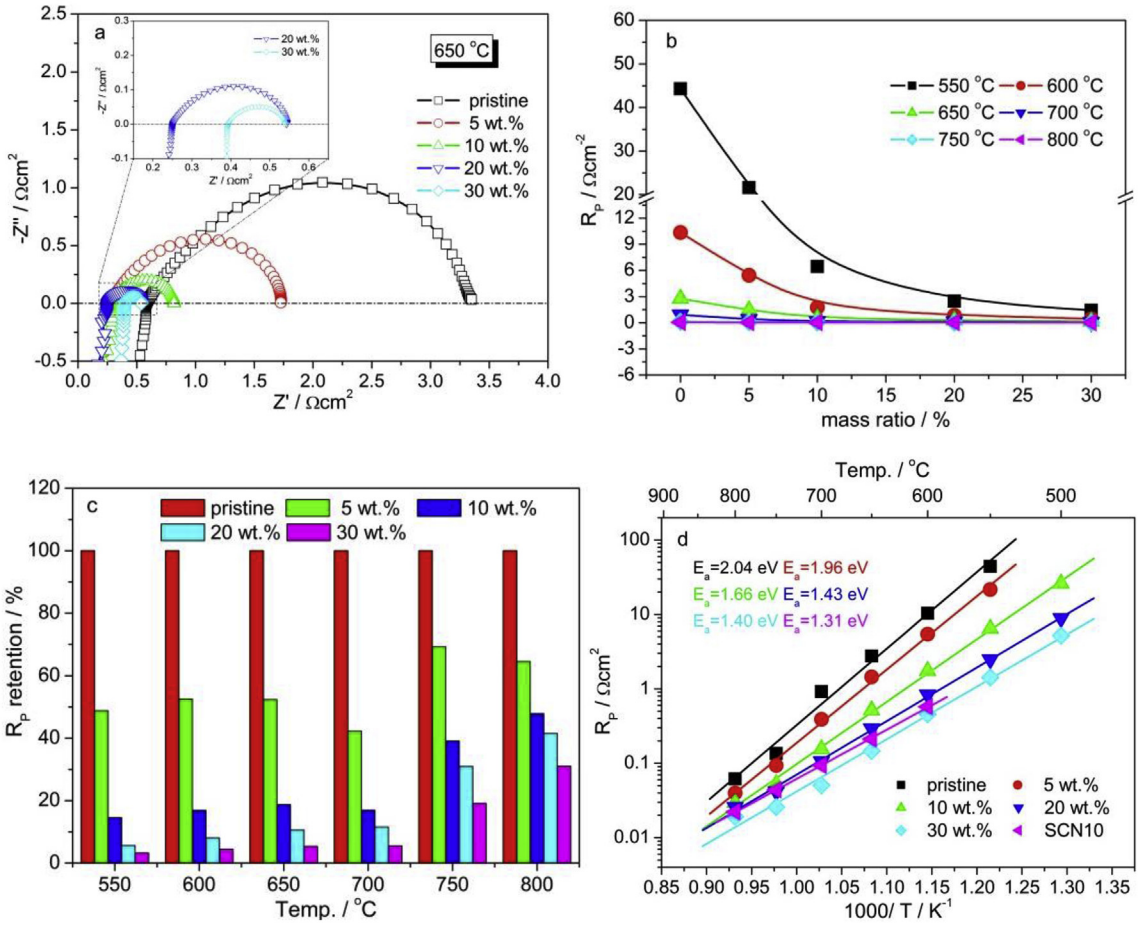


Fig. 4. (a) EIS spectra of pristine LSCF with different SCN10-NPs mass loadings at 650 °C; (b) R_P vs SCN10 mass loadings at the different temperatures; (c) R_P reduction percentage vs temperatures; (d) Arrhenius plot of R_P under different mass loadings.

skeleton.

3.2. The effect of SCN10 loading on R_P

The mass loading effect of SCN10-coating on R_P was evaluated in air from 550 to 800 °C. Fig. 4a shows a representative Nyquist plot collected at 650 °C, from which R_P (the length on the Z′-axis intersected by the arc) is determined. Fig. 4b plots R_P as a function of mass loading at different temperatures. It is evident that R_P decreases with mass loading, but the lower the temperature the more pronounced the

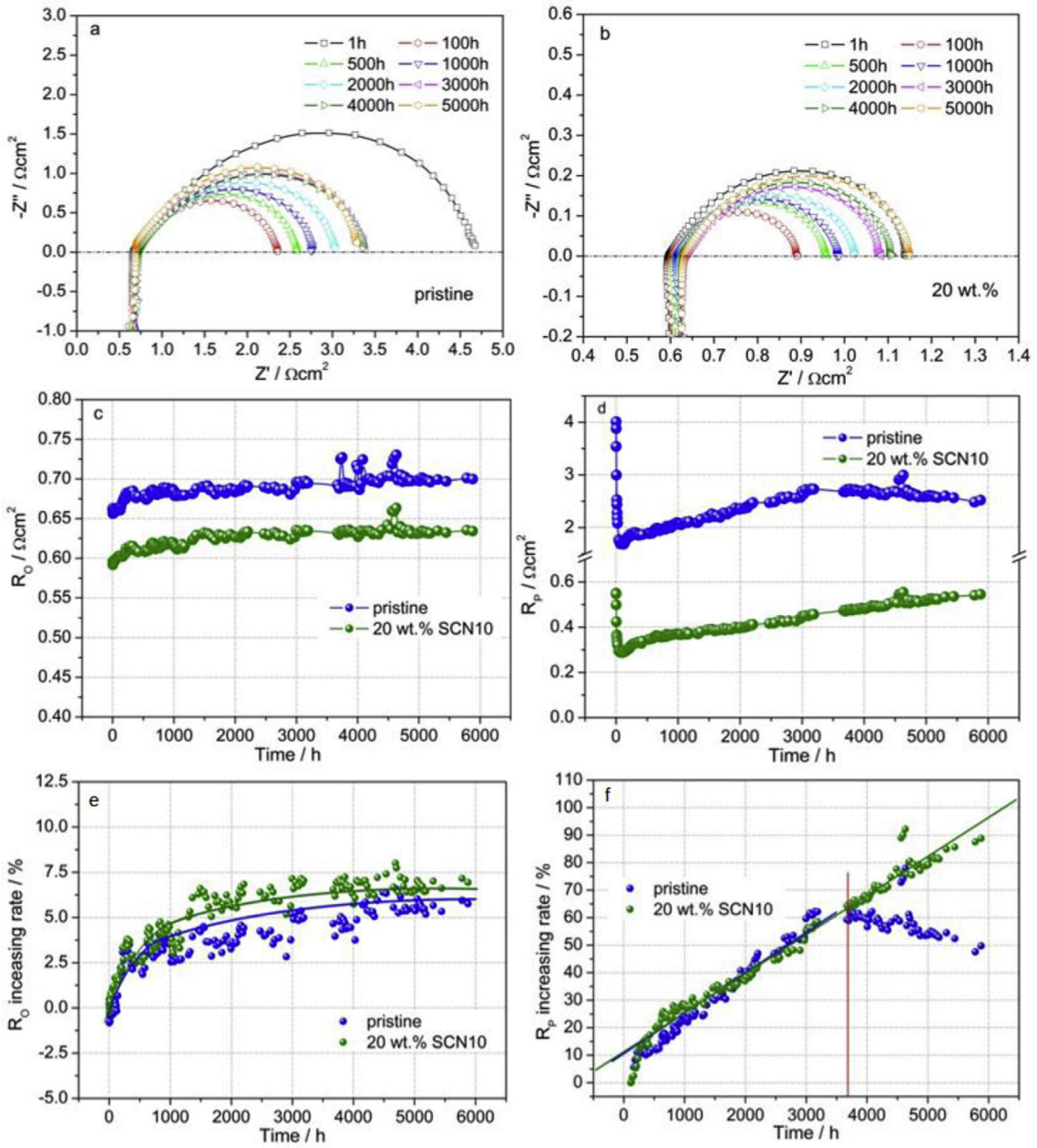


Fig. 5. EIS spectra of (a) the pristine LSCF and (b) 20 wt% SCN10-LSCF cathodes *vs* time. R_O (c) and R_P (d) and their corresponding rates of increase in R_O (e) and R_P (f) *vs* time for the pristine LSCF cathode and 20 wt % SCN10-LSCF cathode, respectively, at 650 °C.

reduction, which is better illustrated by the relative percentage of reduction shown in Fig. 4c. The Arrhenius plots of R_P of cathodes with different SCN10-loadings as well as the baseline pristine LSCF are compared in Fig. 4d with activation energies (E_a) calculated for each sample. As expected, E_a monotonically decreases with loading from 2.04 eV for the pristine LSCF to 1.96, 1.66, 1.43 and 1.40 eV for 5, 10, 20 and 30 wt% loading, respectively. The lowered E_a reflects the promotional effect by SCN10-NPs resulting from significantly increased reactive surface areas and better intrinsic ORR activity. Given the fact that much lower electrode porosity (10%), heavy agglomeration and production unfriendliness at 30 wt% loading, 20 wt% SCN10-LSCF cathode was selected for further investigation. Besides, it is noted that E_a reduction becomes less pronounced as the loading reaches 20 wt%, suggesting that 20 wt% may be the optimal loading for the SCN10-LSCF cathode.

3.3. Long-term stability of R_P

The long-term stability of R_P was evaluated by measuring EIS at a given time interval; Nyquist plots measured at 650 °C are shown as an example for several selected time intervals in Fig. 5a and b, respectively, for the pristine and SCN10-LSCF cathodes. The extracted R_O (ohmic resistance) and R_P are further plotted in Fig. 5c and d, respectively, as a function of time. It should be mentioned that the initial R_O value for the two samples varies slightly due to the electrolyte thickness. For R_O, Fig. 5e, both cathodes exhibit a relatively stable rate of R_O variation over ~6,000 h testing period, whereas the real difference is in R_P. The slight R_O increase could be attributed to: (1) the surface Gd segregation of the electrolyte, in which the surface monolayers of Gd-enriched phase could lead to a sudden surface conductivity shift due to the structural change; (2) the surface Sr-segregation on the cathode [30,31]. For R_P, to better understand the degradation behavior, we divided the entire 6,000 h testing into two periods: (I)100-3,700 h and

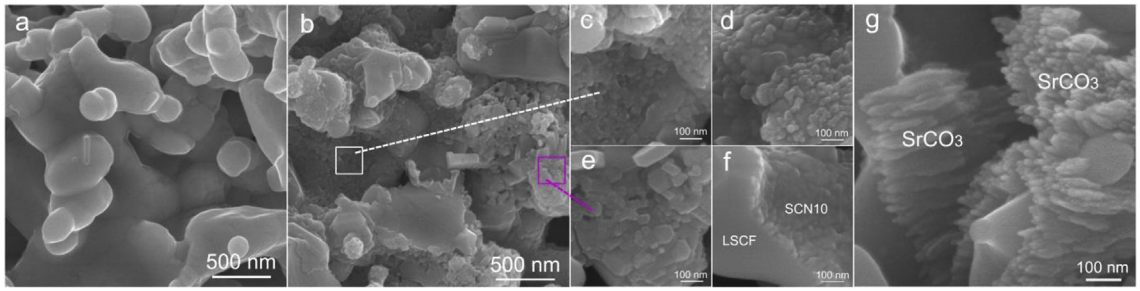


Fig. 6. SEM images of (a) pristine LSCF and (b–g) 20 wt% SCN10-LSCF cathodes after 6,000 h testing.

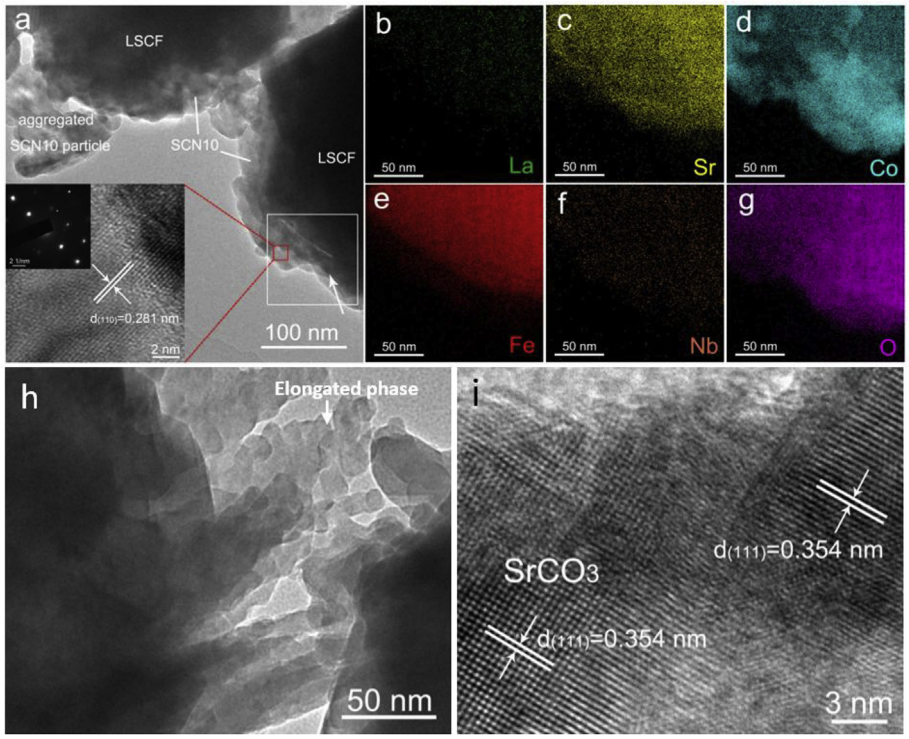


Fig. 7. (a) TEM and (b–g) the corresponding EDS elemental mapping of 20 wt% SCN10-LSCF cathode after 6000 h long-term test; (h) TEM and (i) HRTEM images of the elongated Sr-enriched phase (Fig. 6g) in the 20 wt% SCN10-LSCF cathode.

(II) 3,700–6,000 h. The rapid decrease in R_P during the first 100 h in both cathodes is likely due to the interfacial rearrangement/restructuring, which is very common for SOFC cathodes [32,33]. For Period I, Fig. 5f shows a similar rate of R_P-increase for the pristine and SCN10-LSCF cathodes, *i.e.* 16.3%/1,000 h (or ~ 0.328 Ω cm^2/1,000 h) and 15.6%/1,000 h (or 0.053 Ω cm^2/1,000 h), respectively. For Period II, R_P exhibits a different trending: a continuous increase for the SCN10-LSCF cathode, while stabilized value for the pristine LSCF cathode, even though R_P of SCN10-LSCF bilayer cathode is much lower than that of pristine LSCF. We speculate that this phenomenon is caused by Ag-current collector that penetrates the cathode structure during long-term testing via gas-phase transport. We have confirmed Ag-penetration in our previous work [34]. Ag is known as a good ORR catalyst, which lowers R_P for the pristine sample after Ag reaches a threshold. While Ag also plays a role in SCN10-LSCF cathode, nanoparticles coarsening and formation of $SrCO_3$ still dominate the R_P, resulting in a net increase of R_P in SCN10-LSCF.

3.4. Post-test microscopic/spectroscopic analysis

To understand the long-term behavior, we performed a detailed post-test analysis using SEM, TEM and HRTEM. Fig. 6 shows the morphologies of the two cathodes after 6,000 h testing. In general, the pristine LSCF cathode exhibits a smooth surface (Fig. 6a), while slightly coarsened SCN10 particles in a size of 20–100 nm are observed (Fig. 6b–e). In addition, the SCN10 layer also shows a good interfacial bonding with the LSCF skeleton (Fig. 6f). In some locations, a different elongated SCN10 particle morphology is also observed (Fig. 6g), suggesting a possible new phase formation.

To investigate the phase composition of SCN10-coated LSCF before and after testing, we performed EDS analysis. Fig. 7 shows the results of a combined HRTEM and EDS analysis. Again, the results reveal a nanosized, well distributed and crystallized SCN10 phase with a *d*-spacing of 0.281 nm, matching well with the (110) plane of SCN10; this is like that shown in Figs. 2 and 3. However, a further HRTEM analysis of Fig. 7h–i suggests that the elongated phase shown in Fig. 6g is $SrCO_3$, as the *d*-spacing is 0.354 nm, corresponding to the (111) plane of $SrCO_3$ [35].

Overall, the SCN10 layer maintains in general its original nanosized crystalline morphology, ensuring high specific surface area and good catalytic activity during the 6,000-h testing. In addition, uniform distribution over and a better interfacial bonding to the LSCF backbone also contribute to the stable and active performance. The finding of $SrCO_3$ phase is important, as it signals that Sr in SCN10 can react with

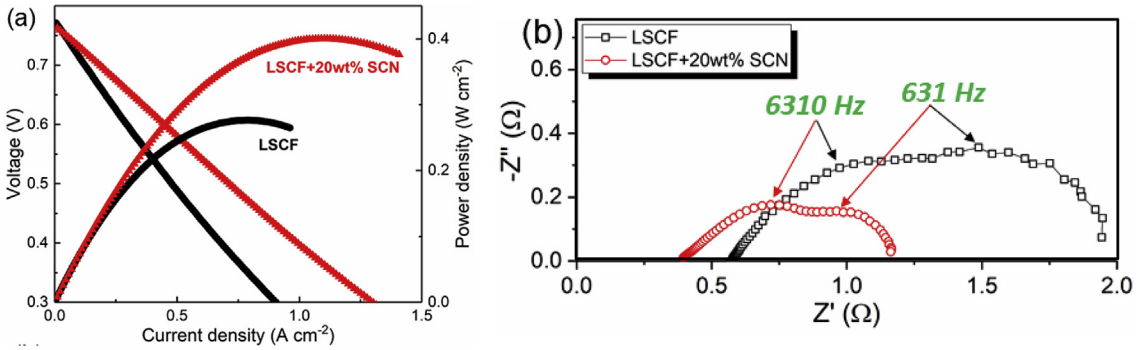


Fig. 8. (a) Voltage and power density versus current density and (b) EIS at OCV for anode-supported full cell at 600 °C.

CO_2 in the ambient air to form detrimental $SrCO_3$, even though the formation kinetics is relatively slow at such a low temperature. Therefore, preventing surface Sr-segregation is necessary to ensure an extended life for SCN10-LSCF cathode. Based on literature and our previous published work, possible strategies to suppress the surface Sr-segregation could be [36–39]: (1) doping A-site with the elements having the smallest size mismatch with the host cation; (2) coating a layer of less reducible oxide over Sr-doped cathode; (3) reducing the surface charge by doping A or B site with higher-valence cations or introducing surface A-site vacancies.

3.5. Full cell performance

Fig. 8a show voltage and power density versus current density at 600 °C for cells with pristine LSCF or 20 wt% SCN-LSCF as cathode. The maximum power density reaches 0.4 W cm^{-2} for infiltrated sample versus 0.28 W cm^{-2} for the pristine one. Fig. 8b shows the Nyquist plot of AC impedance for those two cells at OCV. Infiltration substantially decrease polarization resistance from 1.4 Ω to 0.79 Ω. This is consistent with the R_P observation of symmetrical cells in section 3.2. Ohmic resistance is 0.38 Ω for the infiltrated sample, which is also lower than that of the pristine sample (0.58 Ω). Since the only difference between two cells is the very thin cathode (~25 μm), the smaller ohmic resistance probably arise from the better cathode/electrolyte contact of the infiltrated sample.

4. Conclusions

In summary, we have demonstrated that the ORR activity of a commercial LSCF cathode can be significantly improved by covering a uniform layer of SCN10 on the surface of LSCF skeleton. At 650 °C, R_P reduction has been achieved at 47.7, 81.3, 89.4 and 94.7% with a SCN10 mass loading at 5, 10, 20 and 30 wt%, respectively. A co-analysis of R_P and microstructure suggests that 20 wt% is the optimal value for the SCN10-loading. A long-term stability study on R_P at 650 °C reveals that both the pristine and SCN10-LSCF cathodes exhibit a similar R_P growth rate for the first 3,700 h, beyond which SCN10-LSCF exhibits a higher growth rate. A post-test microscopic/spectroscopic analysis further reveals that the SCN10 layer largely retains its original crystallinity, uniformity and particle size even after 6,000 h testing, but with some sporadic locations filled with $SrCO_3$, which may contribute to the performance degradation.

Acknowledgement

This work was funded by the Advanced Research Projects Agency - Energy, U.S. Department of Energy, under award number DE-AR0000492 and Office of Fossil Energy, U.S. Department of Energy, under award number DE-FE-0023317, and National Science Foundation, under award number of CBET-1464112.

References

[1] S.C. Singhal, Solid State Ionics 135 (2000) 305–313.
[2] B.C.H. Steele, A. Heinzel, Nature 414 (2001) 345–352.
[3] S.C. Singhal, Solid State Ionics 152–153 (2002) 405–410.
[4] L.W. Tai, M.M. Nasrallah, H.U. Anderson, D.M. Sparlin, S.R. Sehlin, Solid State Ionics 76 (1995) 259–271.
[5] L.W. Tai, M.M. Nasrallah, H.U. Anderson, D.M. Sparlin, S.R. Sehlin, Solid State Ionics 76 (1995) 273–283.
[6] E.P. Murray, M.J. Sever, S.A. Barnett, Solid State Ionics 148 (2002) 27–34.
[7] A. Mai, V.A.C. Haanappel, S. Uhlenbruck, F. Tietz, D. Stöver, Solid State Ionics 176 (1995) 1341–1350.
[8] A. Mai, V.A.C. Haanappel, S. Uhlenbruck, F. Tietz, D. Stöver, Solid State Ionics 176 (2005) 1341–1350.
[9] G. Ch Kostogloudis, Ch Ftikos, Solid State Ionics 126 (1999) 143–151.
[10] F. Qiang, K. Sun, N. Zhang, S. Le, X. Zhu, J. Piao, J. Solid State Electrochem. 13 (2009) 455–467.
[11] Y. Teraoka, T. Nobunaga, K. Okamoto, N. Miura, N. Yamazoe, Solid State Ionics 148 (1991) 207–212.
[12] K. Huang, M. Feng, J.B. Goodenough, M. Schmerling, J. Electrochem. Soc. 143 (1996) 3630–3636.
[13] K. Huang, H.Y. Lee, J.B. Goodenough, J. Electrochem. Soc. 145 (1998) 3220–3227.
[14] Z. Shao, S.M. Haile, Nature 431 (2004) 170–173.
[15] W. Zhou, Z. Shao, R. Ran, W. Jin, N. Xu, Chem. Commun. (2008) 5791–5793.
[16] F. Wang, Q. Zhou, T. He, G. Li, H. Ding, J. Power Sources 195 (2010) 3772–3778.
[17] Y. Shen, F. Wang, X. Ma, T. He, J. Power Sources 196 (2011) 7420–7425.
[18] J. Wang, T. Yang, L. Lei, K. Huang, J. Mater. Chem. 5 (2017) 8989–9002.
[19] M. Li, W. Zhou, Z. Zhu, ChemElectroChem 2 (2015) 1331–1338.
[20] A. Aguadero, D. Pérez-Coll, J.A. Alonso, S.J. Skinner, J. Kilner, Chem. Mater. 24 (2012) 2655–2663.
[21] A. Aguadero, J.A. Alonso, D. Pérez-Coll, C. Calle, M.T. Fernández-Díaz, J.B. Goodenough, Chem. Mater. 22 (2010) 789–798.
[22] G. Kim, S. Wang, A.J. Jacobson, L. Reimus, P. Brodersen, C.A. Mims, J. Mater. Chem. 17 (2007) 2500–2505.
[23] A. Chang, S.J. Skinner, J.A. Kilner, Solid State Ionics 177 (2006) 2009–2011.
[24] J.H. Kim, M. Cassidy, J.T.S. Irvine, J. Bae, Chem. Mater. 22 (2010) 883–892.
[25] J.H. Kim, A. Manthiram, J. Electrochem. Soc. 155 (2008) B385–B390.
[26] D. Chen, C. Chen, Y. Gao, Z. Zhang, Z. Shao, F. Giucci, J. Power Sources 295 (2015) 117–124.
[27] R.E. Usiskin, T.C. Davenport, R.Y. Wang, W. Guan, S.M. Haile, Chem. Mater. 28 (2016) 2599–2608.
[28] J. Wang, L. Jiang, X. Xiong, C. Zhang, X. Jin, L. Lei, K. Huang, J. Electrochem. Soc. 163 (2016) F891–F898.
[29] T. Yang, J. Wang, Y. Chen, K. An, D. Ma, T. Vogt, K. Huang, ACS Appl. Mater. Interfaces 9 (2017) 34855–34864.
[30] P.J. Scanlon, R.A.M. Bink, F.P.F. van Berkel, G.M. Christie, L.J. van IJzendoorn, H.H. Brongersma, R.G. van Welzenis, Solid State Ionics 112 (1998) 123–130.
[31] J. Druce, H. Téllez, J. Hyodo, MRS Bull. 39 (2014) 810–815.
[32] K. Lu, F. Shen, Int. J. Hydrogen Energy 39 (2014) 7963–7971.
[33] X. Lou, S. Wang, Z. Liu, L. Yang, M. Liu, Solid State Ionics 180 (2009) 1285–1289.
[34] Y. Gong, C. Qin, K. Huang, ECS Electrochem. Lett. 2 (1) (2013) F1–F4.
[35] W.S. Wang, L. Zhen, C.Y. Xu, L. Yang, W.Z. Shao, Cryst. Growth Des. 8 (2008) 1734–1740.
[36] W. Lee, J.W. Han, Y. Chen, Z. Cai, B. Yildiz, J. Am. Chem. Soc. 135 (2013) 7909–7925.
[37] H. Ding, A.V. Virkar, M. Liu, F. Liu, Phys. Chem. Chem. Phys. 15 (2013) 489–496.
[38] Y. Gong, R.L. Patel, X. Liang, D. Palacio, X. Song, J.B. Goodenough, K. Huang, Chem. Mater. 25 (2013) 4224–4231.
[39] Y. Gong, D. Palacio, X. Song, R.L. Patel, X. Liang, X. Zhao, J.B. Goodenough, K. Huang, Nano Lett. 13 (2013) 4340–4345.